Mechanisms for fragment formation in brittle solids

Artem Levandovsky* and Anna C. Balazs
Chemical Engineering Department, University of Pittsburgh, Pittsburgh, Pennsylvania 15261, USA
(Received 10 November 2006; published 9 May 2007)

A model for mode I fracture in brittle materials is used to elucidate the relationship between characteristics of the fracture process, such as crack roughness, fractal dimension, and fragment size distributions. It is shown that different roughness in local regions of the crack path leads to different mechanisms for the subsequent fracture of those regions. Formation of two robust power laws for the distribution of formed fragments is observed, governing the size distribution of smaller and larger fragments. We connect measurements in fragment size distribution with the local roughness of cracks in the region of fragment formation.

DOI: 10.1103/PhysRevE.75.056105 PACS number(s): 62.20.Mk, 46.50.+a

I. INTRODUCTION

Fracture and fragmentation are ubiquitous processes in materials and understanding these events is not only of fundamental interest, but also is vitally important for a broad range of technological applications. Recent findings suggest that both fracture and fragmentation can be characterized in terms of a few, relatively simple scaling laws [1–7]. Developing a fundamental understanding of the physical underpinnings of these scaling laws, however, represents a significant theoretical challenge. The latter problem is quite difficult because fracture involves complex dynamical behavior that encompasses many different time and length scales. Additionally, the manner in which the experiments are carried out makes certain aspects of crack behavior more or less difficult to measure. Consequently, theoretical research in this area tends to be focused mainly on aspects of fracture having to do with the specific way fracture is initiated in experiments. For example, we now have a relatively well-established understanding about the universality of the crack surface roughness exponent in mode I fracture, both in two- and three-dimensions [1–4], and the power law distribution for fragment sizes in fracture by impact [5–7]. Much less, however, is known about the relationship between scaling laws in these two types of fracture, or about the roughness of fragments produced via impact fracture. Different explanations for these respective power laws were proposed, but a full theoretical understanding of fracture dynamics is far from complete. Additionally, while the multifractal character of fracture is generally accepted [8], it is not well-established which features of crack growth can be explicitly characterized in terms of fractal analysis [9].

In this paper, we focus on mode I fracture (where the tensile stress is normal to the line of the crack) in brittle materials through use of a simple model, which nonetheless produces rich behavior in terms of multifractal crack, patterns, fragment formation, the coexistence of smooth and rough cracks, and different types of structural evolution for regions with predominantly rough and smooth cracks. By utilizing such simple models that nevertheless generate sufficiently rich behavior, one can connect different aspects of fracture, such as crack roughness and fragment formation, and thereby produce a more unified description of the events.

The paper is organized as follows. We develop a model of fracture, discuss the fracture criterion, and describe the simulations in Sec. II. In Sec. III, we consider cracks in strips of two different materials and analyze the coexistence of regions of both smooth and rough cracks that appear in these materials. We also predict the different ways these distinct regions will continue to evolve with further fracture. We then numerically analyze the crack evolution and arrive at two different power laws for the fragment size distribution. We propose an explanation for the origin of the differences in the values of the power exponents. We also provide some discussion of possible influences of experimental measurements that are not described by our model, and arrive at our conclusions in Sec. IV.

II. MODEL DESCRIPTION

In this section, we describe the general framework of our model of crack propagation in thin brittle plates undergoing mode I fracture. The model is based on a theory of linear elasticity and incorporates the maximum eigenvalue of a strain tensor as a fracture criterion for crack growth. To construct the model, we consider deformations that (1) occur in the plane of a finite two-dimensional plate and (2) do not result in any bending of the plate. Below, we outline a method for discretizing this model in the special case of thin plates.

The evolution of the displacement field $\vec{u}(\vec{r},t)$ in a homogeneous material is governed by the following equation [10]:

$$\ddot{\vec{u}}(r,t) = c_{\perp}^2 \nabla^2 \vec{u}(\vec{r},t) + (c_{\parallel}^2 - c_{\perp}^2)\vec{\nabla}[\vec{\nabla} \cdot \vec{u}(\vec{r},t)], \qquad (1)$$

where $c_{\perp}$ and $c_{\parallel}$ are the respective transverse and longitudinal speeds of sound. The latter quantities are material parameters related to the Young's modulus E and Poisson's ratio ν. If the plate is sufficiently thin, the deformation can be regarded as being uniform over the thickness of the material. The strain tensor is then solely a function of x and y (with the plate being oriented in the xy plane). The boundary conditions for components of the stress tensor at both surfaces of the plate are then $\sigma_{xz}=\sigma_{yz}=\sigma_{zz}=0$. Consequently, the nonzero components of the stress tensor in terms of the strain tensor are

*Corresponding author. Electronic address: arteml@yahoo.com

$$\sigma_{xx} = \frac{E}{1-\nu^2}(u_{xx} + \nu u_{yy}),$$

$$\sigma_{yy} = \frac{E}{1-\nu^2}(u_{yy} + \nu u_{xx}), \tag{2}$$

$$\sigma_{xy} = \frac{E}{1+\nu} u_{xy}.$$

Here, the strain tensor is given by $u_{ij} = \frac{1}{2}\left(\frac{\partial u_i}{\partial x_j} + \frac{\partial u_j}{\partial x_i}\right)$. For the special case of small plate thickness h, the following transformation allows us to consider Eq. (1) to be a two-dimensional vector form, with all the vector operators being two-dimensional:

$$c_\perp^2 = \frac{Eh}{2\rho(1+\nu)},$$

$$c_\parallel^2 = \frac{Eh}{\rho(1-\nu^2)}, \tag{3}$$

where ρ is the surface density of a material, defined as mass per unit area.

It can be shown that a two-dimensional lattice model with a bond bending term, as developed in Ref. [11], recovers the dynamical equations of motion, Eq. (1), up to second order in the lattice spacing. The following Hamiltonian defines this lattice model [11]:

$$H = \sum_i \frac{p_i^2}{2m} + \frac{1}{2}\sum_{ij} k_1[(\vec{u}_i - \vec{u}_j)\hat{x}_{ij}]^2 + \frac{1}{2}\sum_{ij} k_2[(\vec{u}_i - \vec{u}_j)\hat{x}_{ij}]^2$$

$$+ \frac{c}{2}\sum_{ijl} (\cos\theta_{ij,il} - \cos 45^\circ)^2, \tag{4}$$

where $\hat{x}_{ij}$ is the unit vector. In Eq. (4) p_i is a momentum and m is a mass associated with a node.

We construct a lattice model that is described by Eq. (4). In particular, the interactions between the nodes on the lattice are characterized by three force constants: nearest- and next-nearest-neighbor central interactions with constants k_1 and k_2, respectively, and a next-nearest neighbor bond-bending interaction with constant c [see Fig. 1(a)]. Central interactions control bond stretching and noncentral interactions govern the displacement of each of the eight angles θ made by the adjacent nearest neighbor, central node, and next-nearest neighbor [see Fig. 1(a)]. The relationship between the force constants and material parameters are given by

$$E = 8k(k + c/a^2)/(3k + c/a^2),$$

$$\nu = (k - c/a^2)/(3k + c/a^2). \tag{5}$$

By setting $k = k_1 = k_2/2$, we recover the isotropic properties of the medium [11]. The noncentral, bond bending term is required if one wants to account for varying material properties. Setting $c=0$ fixes the Poisson's ratio at $\nu = 1/3$.

Formulation of a problem as in Eq. (4) allows us to carry out numerical simulations of the dynamic behavior of the system by means of molecular dynamic algorithms. The main advantage of formulating a dynamic model in this manner, rather than using Eq. (1), is that it allows us to avoid numerical stability problems pertinent to Eq. (1).

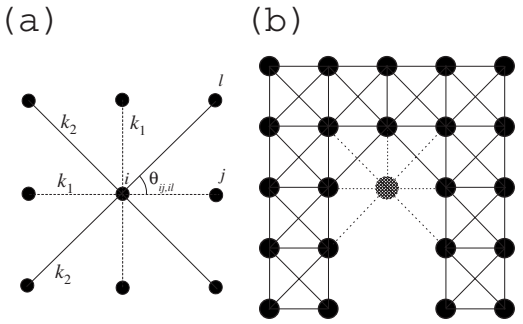

FIG. 1. (a) The central node interacts by means of a central force with four nearest and four next-nearest neighbors connected by springs with spring constants k_1 and k_2, respectively, and a noncentral force, depending on eight angles θ (only one shown), formed by nearest, central, and next-nearest neighbors. (b) The crack (void at the bottom) propagates through the nodes. After the shaded node is removed, the crack will advance one step in the upward direction.

A. Fracture criterion

The criterion for the propagation of fracture is a crucial component of the continuum simulation of the fracture dynamics. The physical representation of a material breaking is usually implemented through the commonly used *most stretched bond rule* (see, e.g., [9] and references therein). In this paper, we implement a fracture criterion not on the bonds between nodes, but on the nodes themselves. In particular, we use the maximum eigenvalue of the strain tensor at a node as the criterion of fracture [12]. If the maximum eigenvalue of the strain tensor at a node exceeds the threshold value γ^*, the node no longer interacts with its neighbors and a crack is considered to be propagating through that node, as shown in Fig. 1(b).

Since cracks propagate through the nodes, one always has all the components of the strain tensor measured at the place where the crack would go, before making the decision to advance the crack. If a fracture criterion were to be implemented on the bonds, only one component of the strain tensor could be measured directly. The other components would have to be interpolated from information collected from the vicinity of a bond or averaged from a group of bonds.

This current formulation of the fracture criterion makes it possible to preserve symmetry with respect to a crack line, in straight propagating cracks. This allows us to partition the fracture modes and focus on mode-I fracture. Elimination of mode-II perturbations significantly reduces lattice-trapping effects. In this manner, the shape and dynamics of the tensor fields obtained from the simulations can be analyzed efficiently.

B. Simulation procedure

We study mode I fracture in two-dimensional plates by carrying out conventional molecular dynamic simulations of

the nodes' equations of motion, as obtained from Eq. (4). The following procedure is used to initiate the simulations. A fixed strain of 1% is applied to the vertical sides of a plate, i.e., the nodes at $x=0$ and $x=N_x a$, where N_x is the node number and a is the lattice spacing. The crack is initiated at the midpoint of the top plate (at $x=aN_x/2$) by breaking a set of nodes to produce a vertical "cut." After this cut is made, the simulations are carried out until the system reaches equilibrium. At this stage, the simulations are performed with a dissipative force ($F \propto -\dot{\vec{x}}$), which is added to the model given by Eq. (4). The plate's utmost left and utmost right nodes, with coordinates $x=0$ and $x=N_x a$, are allowed to move in the vertical direction to eliminate strain concentrations at the corners of a plate. After all nodes are effectively at rest, we record the value of the maximum eigenvalue of the strain tensor γ^* of the most overloaded node and use this value as a critical value in further simulations. Our typical value is $\gamma^*=2.5\%$. The dissipative forces are turned off after this initial stage. The simulations are then carried out from the equilibrium configuration obtained from the first stage, with nodes at $x=0$ and $x=N_x a$ being allowed to move in the vertical direction while being kept at fixed horizontal displacement.

Our model describes crack growth as a fully deterministic process. Keeping the symmetry of the crack with respect to the $x=aN_x/2$ line serves two purposes: it allows us to exclude mode II perturbations and facilitates the observation of the crack evolution, which otherwise would require additional statistical analysis.

III. RESULTS AND DISCUSSION

A. Origin and nature of the fragmentation process

The crack morphology is usually analyzed in terms of one of the following: the fractal dimension, surface roughening, or fragment size distributions. We begin our analysis of these descriptions of the crack morphology for mode I fracture in two dimensions by discussing cracks in long strips of material, as shown in Fig. 2.

Here, we highlight the connection between temporal trends in the crack growth (fragmentation of plates after primary crack development) and the much less considered, alternating spatially localized patterns (roughness of primary crack). We consider cracks in two materials, one with a Poisson's ratio of $\nu=1/3$ (where $c=0$), as shown in Fig. 2(a), and another with $\nu=1/5$ (where $c=0.2$), as shown in Fig. 2(b).

The cracks propagate from top to bottom and the patterns are given for the time it takes the dominant cracks to reach the bottom of the plates. For completeness, we note here that the y-component of the crack velocity remains constant. The cracks start as a straight line, undergo a branching bifurcation, develop two or more branches, and sometimes create closed loops (i.e., fragments). In Fig. 2, the fractal dimension of both samples is close to 1.30, though some local regions in Fig. 2 contain parts with both higher and lower values. Parts of the strip with rough crack surfaces (R_1 in Fig. 2) alternate with parts of the strip with much smoother cracks (R_2 in Fig. 2). This point can also be seen in Fig. 3, where we plot the fractal dimension of the crack along the y direction.

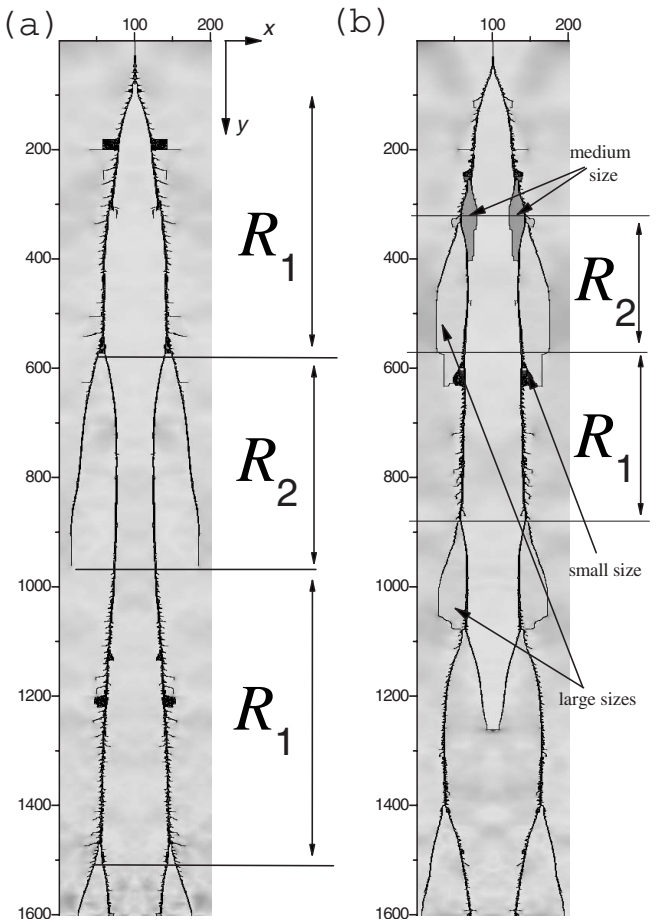

FIG. 2. Cracks in a strip of material with Poisson's ratio $\nu=1/3$ (a) and $\nu=1/5$ (b). Patterns are given in the background of a strain field; the darker the color, the higher the value of strain field. Alternating regions R_1 and R_2 occupied by cracks with higher (more than 1.30) and lower fractal dimensions, see Fig. 3. The shattering process [almost black spots, like the one at $y=200$ in (a)] is more pronounced in the region of higher fractal dimension. The fragments at $y=300$ in (b) have a higher strain value than larger fragments, implying that cracks inside smaller fragments are likely to happen somewhat sooner than possible further fragmentation of the bigger fragments in (b).

The origin of the local character of the crack roughness in Fig. 2 lies in a crack branching instability. Unlike the first branching bifurcation at $y=90$, where two branches were related by symmetry with respect to the vertical line ($x=100$) perpendicular to the applied strain, the subsequent branching bifurcation is affected asymmetrically by the applied deformation. The branches that are oriented more along the vertical direction are favored by the flow (i.e., redistribution) of elastic energy and branches oriented more perpendicular to this direction become abandoned. As the two main branches become sufficiently separated, their behavior starts to resemble that of the initial crack on top of Fig. 2; the main difference is that the flow of elastic energy toward each branch is limited by the number of neighboring branches.

It is possible to choose the width of a strip to be exactly the size to support only two branches, which would orient

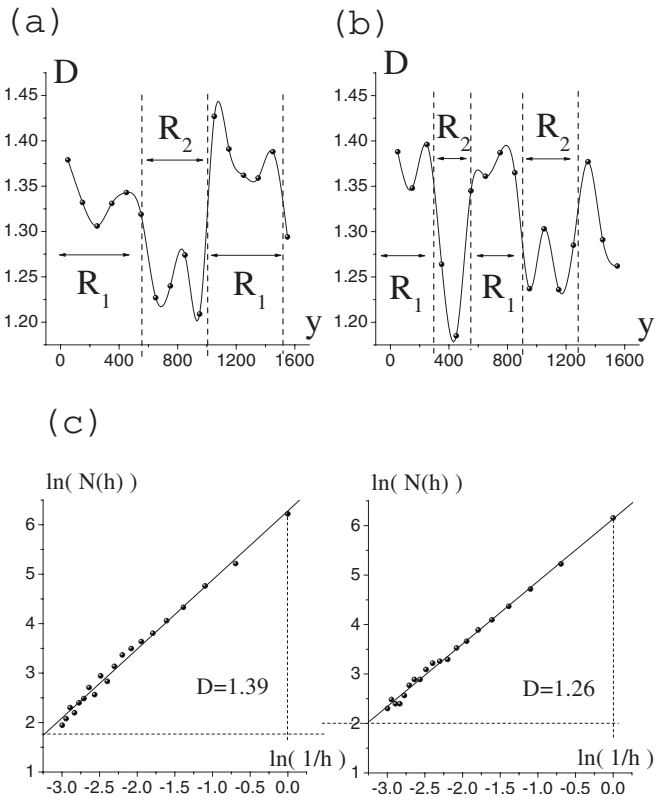

FIG. 3. (a) and (b) Local fractal dimension (D) of cracks [in Figs. 2(a) and 2(b)] exhibits alternating character along the crack path (i.e., y direction). (c) Fractal dimension obtained by a box counting method as the slope of the graph of $\ln[N(h)]$ vs $\ln(1/h)$, with the size of a box h changing from 1 to 20. The plots in (c) are for two points in (b): $y=250$ and 350. Measurements are taken from 16 squares of 100×100 nodes along the crack path at times immediately following the propagation of the main crack through individual squares. Undulations of the fractal dimension in R_1 and R_2 areas [(a) and (b)] are mostly due to the partitioning of the crack path into 100×100 squares, so that some of the squares contain both smooth and rough cracks [see, for example, parts $200<y<300$ and $300<y<400$ in Fig. 2(b)].

themselves parallel to the $x=100$ line. In this case, the amount of energy each branch receives is just the bare minimum needed for crack propagation. In Fig. 2(a), the width of the strip is chosen to be sufficiently wide to store enough elastic energy to support more than two branches, but not wide enough to accommodate four vertical branches. Note the divergence of the four branches at $600<y<900$ until the lack of energy flow towards the outside branches causes a slowing down of these branches. The outside branches then get overtaken by the inside ones, lose their energy supply, and eventually stop growing.

An increase of energy flow towards the two surviving branches at $1000<y<1500$ leads to a number of attempted bifurcations in this region. Note that in the region of $1000<y<1500$, the two branches keep separating from each other and the character of the crack roughness changes as more of the energy supply from the strip center (i.e., directed outwards from the center line $x=100$) becomes available for the crack. The crack roughness develops predominantly on the outside of the branches at $y=1000$, but as the energy flow towards the branches from the left becomes comparable to that from the right, roughness appears on both sides of the branches in the region of $1300<y<1500$ of Fig. 2(a). In the region of $600<y<900$, the small distance between the cracks limits the amount of stored energy per crack, and only smooth surfaces appear.

The process of crack growth in Fig. 2 undergoes oscillation between one pair of rough cracks that tend to expand outward until successfully branching into two pairs, and two pairs of cracks competing for available elastic energy that eventually leads to one winning pair, which develop roughness as soon as the other pair is abandoned.

It was noted previously [12] that crack evolution does not necessarily stop at the moment when the crack arrives at the bottom of a plate, where the material is split into two or more pieces and the external forces applied at vertical boundaries are no longer the primary source of crack growth. Below, we describe in more detail the crack evolution that might be classified as a different phase of crack growth. As we noted, the limited amount of stored energy in the strip prevents cracks in Fig. 2 from undergoing large scale structural reconstruction, but, as we describe below, it is possible to see in which direction this reconstruction will go.

We find that parts of the strips with different roughness (or different fractal dimension), marked as R_1 and R_2 in Figs. 2 and 3, will evolve differently. The regions with rough cracks of higher fractal dimension of 1.35 evolve much faster than those with a fractal dimension of smaller value, below 1.25. The former cracks produce small closed loops; the creation of these closed loops is facilitated by the rough nature of the crack. The fragments that are disconnected from the main plate might undergo further rapid fragmentation, producing debris. Such debris can be found at $y=200$ and 1200 in Fig. 2(a) and at $y=600$ in Fig. 2(b). We point out that the shattering stage here occurs soon after fragment formation. For example, fragments at $y=1200$ in Fig. 2(a) get shattered before the branches of the main crack (whose propagation is assisted by external forces) arrive at the bottom of the plate.

Fragmentation of parts associated with the smooth crack happens in a different fashion. It takes more time to produce these fragments and the size of the fragments is generally much larger than the ones in the R_1 region. After a fragment is formed, it might survive without further fragmentation for a considerably longer time than fragments in R_1. We note that the size of the fragments appears to be related to a surviving time (time from fragment formation until further fragmentation). We can see two pairs of relatively large sized fragments at $y=500$ and 1000 in Fig. 2(b) without signs of further fragmentation or debris formation, and we expect the possible formation of one pair of even larger sized fragments that are still connected to the main plate at $600<y<900$ in Fig. 2(a) and the pair of medium fragments $y=300$ in Fig. 2(b). It appears that these medium sized fragments are going to undergo some transformation (further fracture) if the simulations were continued. This is inferred from the higher strain fields inside the fragments, as shown by the darker color in Fig. 2(b). Thus the medium sized fragments appear to evolve much slower than the small fragments and slightly faster than the large ones.

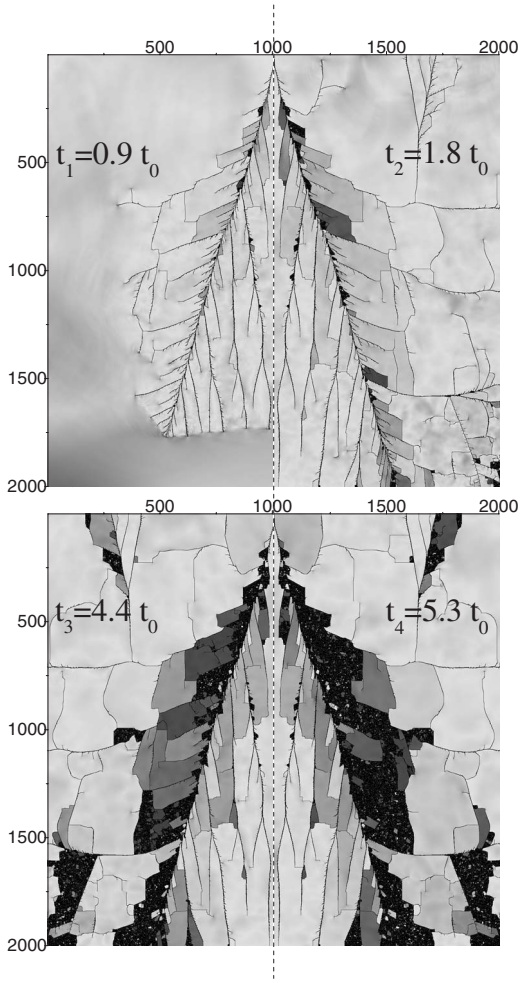

FIG. 4. Snapshots of four half-plates representing the time evolution of a fractured plate as time progresses from t_1 to t_4. Shattered areas appear almost black due to the high concentration of cracks. A darker color indicates a higher strain value. Black lines are the cracks.

B. Fracture pattern formation

We see that fracture in the strip leads to the formation of regions with different fractal dimension. We find parts with fewer branches of higher roughness and fractal dimension and parts with more cracks with smoother surface and smaller fractal dimension. With time, patches of higher fractal dimension exhibit a tendency to evolve faster into a state with even higher fractal dimension, e.g., a value of 1.82 in the vicinity of the shattered loop at $y=200$ in Fig. 2(a). Parts with smooth cracks can evolve into a state with large fragments that are more stable against further fragmentation and shattering. These tendencies are ultimately responsible for the formation of two different scaling laws for the fragmentation process elucidated below.

In Fig. 4 we present a larger sample of 2000×2000 nodes, where we show the time evolution of a crack during a time $5.3t_0$. Time t_0 is defined as the time it takes to form a treelike structure that reaches the bottom of the plate and so splits the plate. The material is the same as the one in Fig. 2(b), with a Poisson's ratio of $\nu=1/5$. Due to the fact that we preserve mirrorlike symmetry with respect to the line $x=aN_x/2$, the left and right parts of a crack can be considered interchangeably. The time evolution of a crack in Fig. 4 is given as four half-plates of a single fractured plate, where each half-plate corresponds to a given time t_n. The structural evolution of the crack is more complex than in Fig. 2. Fragments are often comprised of unequal numbers of rough and smooth sides. So subsequent fragmentation can start at the rough sides of a fragment, produce both rough and smoother new surfaces, and stimulate different evolution trends within the newly formed fragments. Also the "elastic ejection" of a fragment [15] can produce additional strain on the material due to the angular rotation of a fragment. We note that Fig. 4 is designed to show the development of a crack, so that the crack path is easily observable. In Fig. 4, the fractured plate is shown in a Lagrangian (material) system of coordinates where the spatial coordinate of each material point is kept constant as the material deforms or moves.

The fractal dimension of the sample varies significantly with both time and location, from one part of the plate in Fig. 4 to another. The fractal dimension ranges from 1.20 in t_1 in Fig. 4 to 1.82 in later stages of crack growth. It can be seen from Fig. 4 that the fragmentation process develops primarily in places of higher local fractal dimension (crack roughness), as along the "stem of a tree" seen in the t_1 and t_2 frames in Fig. 4. It is also visible in Fig. 4 that crack evolution, like further fragmentation and shattering, is faster in smaller fragments.

We find that the two fragmentation trends discussed earlier with respect to Fig. 2 ultimately lead to two scaling laws for the fragment size distribution. In Fig. 5, we document the robustness of these power laws by plotting the fragment size distribution for earlier and later times of crack growth. We find that the cumulative number of fragments N that are larger than a given area s, $N(>s)$, obey a power law distribution $N(>s)\sim s^{-\alpha}$. The value of the exponent for small fragments is $\alpha\approx0.8$. In this case, the behavior of the system is governed by fragment formation, as in the region of rough cracks, with a higher fractal dimension of 1.35 (as discussed above). For larger fragments (area larger than critical value s^* in Fig. 5) formed by smoother cracks (with a fractal dimension that might approach that of a straight line), the value of the exponent is $\alpha\approx0.3$. The parameter s^* is determined as the crossover between the best fits for the corresponding larger and smaller fragments. We note that the value of the measured exponents depends on how one treats the crossovers between the different regions in Fig. 5 (the crossover at s^* and the cutoff at large s). The sharp crossovers yield the values quoted above. A difference of up to 10% can be measured for a smoother transition at the critical point s^* and at the cutoff at large s due to the characteristic "wave" of measured values (dots in Fig. 5) along the fitted exponents (lines in Fig. 5).

With time, as the number of fragments keeps increasing and a larger area of the plate undergoes a transition to the shattered stage, the size distribution still conforms to the above laws, with the critical value s^* increasing with time. The part of the size distributions with an exponent of 0.8 envelops more fragments with time and includes those of a larger size (see Fig. 5). At each given time t, the critical

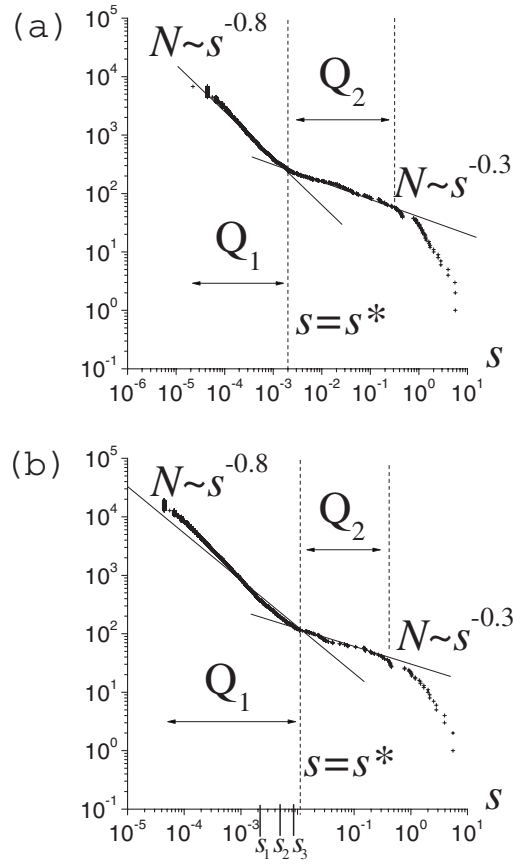

FIG. 5. Fragment size distribution at an earlier time $t=3t_0$ in (a) and at the later $t=4t_0$ (b), measured for the sample in Fig. 6. Fragment size s (in percent of total area of a sample) increasing from left to right. N shows the number of existing fragments with area higher than s. Small sized fragments (to the left of s^*) obey a different scaling law than larger fragments (to the right of s^*). Pertinent to Q_1 set S_n is the same as in Fig. 6.

value s^* is associated with a certain length scale of a fractured plate s_t. Length scales of a plate form a set S_n discussed later in Fig. 6 and shown for comparison in Fig. 5.

We are now in a position to address the question of why there are two distinctive scaling exponents α observed in our stimulations. We found that these exponents are associated with different regions of the fractured plate. Using the concept of critical size s^*, it is possible to pinpoint the location of these regions denoted as Q_1 and Q_2 in Fig. 6. The fragments formed in the Q_1 and Q_2 regions shown in Fig. 6 are mainly contributing to the respective parts of the size distributions in Fig. 5, which are also denoted as Q_1 and Q_2. We note that the shape of fragments in the Q_2 region is mostly that of a rectangle with a low aspect ratio. This is in contrast to the highly elongated shape of some fragments in Q_1.

The Q_1 region is principally associated with a region where the fracture process is driven by the preexisting strain (see Fig. 6). The further evolution of this region in terms of fragment formation is determined by the fractal dimension of the primal crack in Q_1. This crack "carves out" future fragments, so that up to roughly 75% of a fragment perimeter is determined at the initial stage. This is shown in Fig. 6(b), where the set of characteristic length scales S_n determines the typical size of the fragments, with small fragments usually being formed first. As we noted above and in Fig. 5, the part of the size distribution with the exponent of $\alpha \approx 0.8$ envelopes fragments characterized by the same set of length scales S_n, with the critical value s^* moving from smaller sizes of S_n towards s_0, which is the maximum possible value of a set.

The fracture of the secondary region Q_2 is driven mostly by redistribution of energy in the form of emitted (mostly in Q_1) elastic waves. Cracks in Q_2 have a lower fractal dimension and are characterized by another set of length scales, with all length scales being larger than s_0 [compare Figs. 6(b) and 6(c)]. The finite size of a plate limits the amount of initially stored energy in our simulation (and thus the number of fragments formed in the Q_2 region of Fig. 6) and leads to the formation of a two-mode power law distribution in fragment sizes. Nevertheless, the redistribution of energy in the form of elastic waves can lead to the establishment of new tree "stems" [small regions Q_1 in Fig. 6(a), to the right] that reduce the Q_2 region even further, leading to the shrinking of the region governed by the $\alpha \approx 0.3$ exponent in Fig. 5. One would expect that if more than one crack is initiated and/or sustained by an applied strain, the Q_2 region might disappear altogether (and correspondingly, the region governed by exponent $\alpha \approx 0.3$ in Fig. 5).

We can compare our description of composite power laws in fragment formation in mode I fracture found here with experiments on fragmentation by impact. The main difference in the nature of these two types of fragmentation lies in the supply of energy that primarily sustains crack growth (potential energy associated with applied strain here and kinetic energy brought by impact). The composite power laws associated with small and large fragments were indeed seen in the experiments on *low* velocity impact [16], whereas only the power law for small fragments was observed in experiments on *high* velocity impact [6,17]. This disappearance of the power law for larger fragments with an increase in the energy supply (and so an increase of the role of the region associated with primary crack growth, Q_1 here) is associated with the disappearance of the secondary (Q_2 here) region of crack growth. In our simulation, we demonstrate the trend of the Q_2 region to shrink with time.

We note that our exponent of $\alpha \approx 0.3$ lies very close to the experimentally measured exponent of $\alpha \approx 0.35$ [18] obtained in experiments on the fragmentation of thin shells by impact and by explosion. It was suggested that such a relatively small value of the exponent can indicate a cleavage mechanism of fragmentation, which is significantly different [19] from the experimental and theoretical results on fragmentation of two-dimensional bulk systems where $0.5 \leqslant \alpha \leqslant 1$ were found (see Ref. [19] and references therein). The theoretical prediction of the branching-merging process of cracks [20] governed by the existence of defects in the sample gives the lowest exponent in that range, i.e., $\alpha \approx 0.5$. In contrast to a defect-governed process, our model is based on the branching instabilities of cracks propagating in a sample that contains no defects. It was noted that small fragments produced due to such branching instabilities might have a significant effect on the fragment size distribution [21]. Our exponent of $\alpha \approx 0.3$ (obtained in the process of branching and merging of

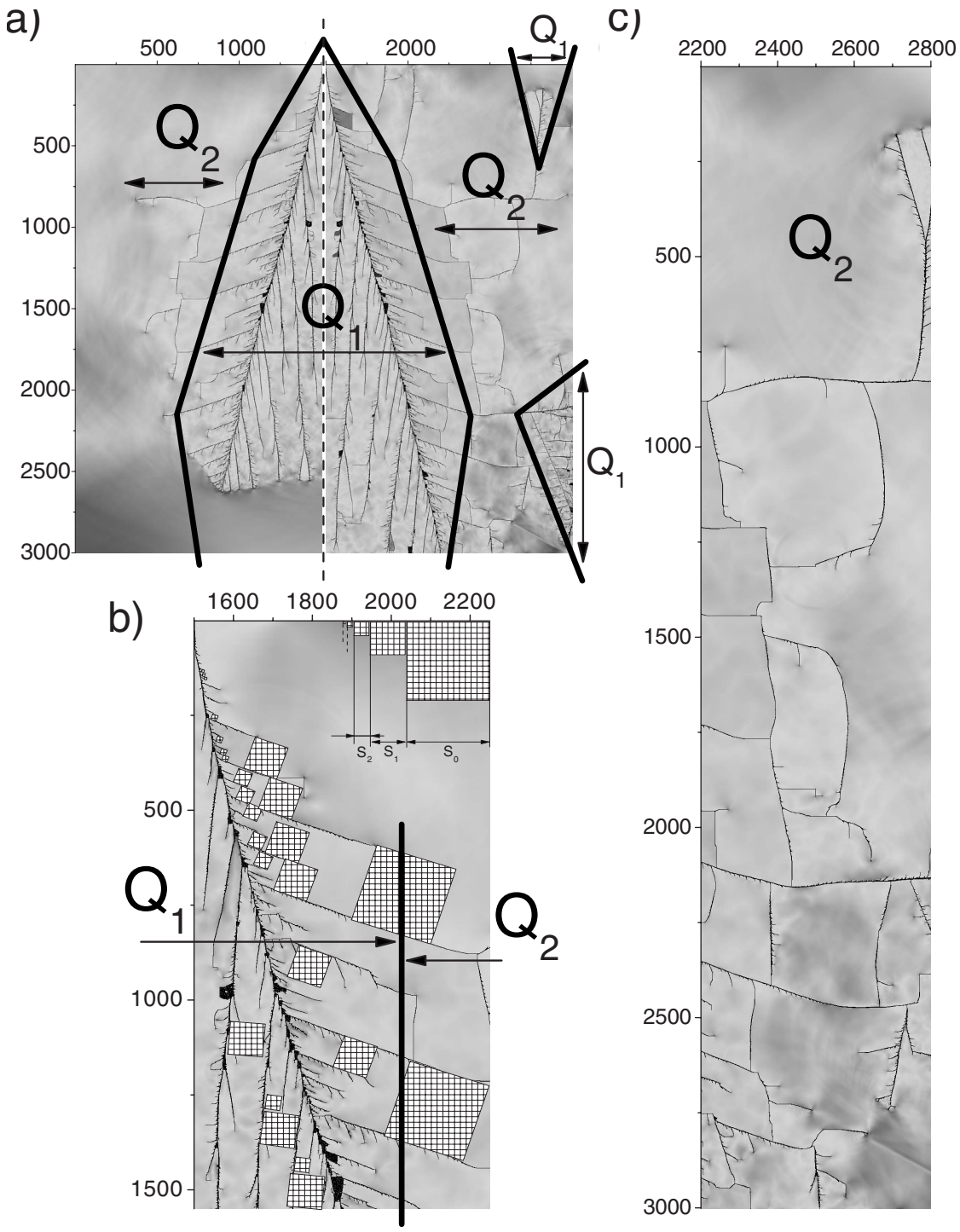

FIG. 6. (a) Two regions of crack growth before and shortly after t_0. (b) Q_1 is associated with rough cracks closer to a "stem" of a tree. It exhibits a set of length scales S_n. The maximum value of this set S_0 is also a characteristic length scale of Q_2, where the other length scales are typically larger than S_0 (c). Parts (b) and (c) are drawn to scale.

deterministic cracks in defect-free samples) might account for the most basic mechanism producing such a low exponent, which was experimentally observed in the fragmentation of thin shells. In addition to the similarity in exponents (close to 1/3), there is a noticeable qualitative similarity in the treelike patterns in our work (see Fig. 6) and the treelike patterns in the experiments on the fragmentation of these thin shells (see Fig. 1 in Ref. [5]).

We find that the same scaling laws discussed above for the sample with $\nu=1/5$ in Fig. 4, and with $\nu=1/3$ in Figs. 5 and 6 holds for a wide range of Poisson's ratios with the exception of very small ($\nu<0.1$) and possibly large ($\nu>0.33$) values. In the range $\nu<0.1$, only one scaling exponent was observed. Unlike the time-independent nature of the scaling exponent for the range $0.1<\nu<0.33$, the value of exponent in the range $0<\nu<0.1$ becomes a function of

time. In particular, the scaling exponent gradually increases with time, approaching the $\alpha \approx 0.8$ value. We also note that formulation of the problem in Eq. (4) limits the investigation to values of the Poisson's ratio lying within the $0 < \nu < 0.33$ range.

To facilitate future experimental studies, it is worth highlighting some issues that should be considered in comparing our present findings (Figs. 2–6) with potential experimental results. In particular, the model does not account for energy dissipation due to processes such as acoustic emission and generation of thermal energy. Inclusion of wave attenuation usually leads to a slowing down of the crack velocity and has a general stabilizing effect against crack branching and growth [13,14]. For sufficiently large samples and fast fracture, the emission of energy in the form of elastic waves is expected to go faster than the dissipation of energy along the crack path; thus the dispersion of elastic energy by elastic waves might be sufficient to allow us to ignore the small dissipation. In one of our simulations, we introduced the absorption of elastic waves (by introducing small dissipative forces) along small strips at the boundaries at $x=0$ and $x=N_x a$. We did not observe any significant decrease in shattering in that particular study and expect the fragmentation process to continue, at least until some critical small size where attenuation of elastic waves might become important.

We also note that in our model, the fragments do not interact with each other. After their formation, they are subject to rotation, additional stress associated with angular motion, and further fracture. In physical experiments, a plate can remain in one piece even if it contains several cracks due to the roughness of crack surfaces and interlocking of the fragments. Such fractured plates can behave almost as if undamaged, at least with respect to compressive deformations. This has a stabilizing effect against the shattering process. We expect that even though such a stabilizing effect might restrict the area of debris formation, the shattering process is still governed by the initial roughness of the cracks, with two types of cracks (rough and smooth) evolving into the formation of, respectively, smaller and larger fragments.

IV. CONCLUSIONS

We used a model of mode I fracture in brittle materials to elucidate the relationship between parameters used to characterize the fracture process, such as crack roughness, fractal dimension, and fragment size distributions. We showed that differences in the local crack morphology (different roughness in local regions of the crack path) are connected to the subsequent crack evolution (further development of the fragmentation) and elucidated different pathways for the evolution of an initially fractured surface. We showed that local differences in the crack morphology lead to the formation of two robust power laws for the distribution of formed fragments, one being pertinent to smaller fragments and one to larger fragments. Tracing the evolution of mode I fracture in surfaces allows us to connect the most commonly measured crack characteristics used in different types of fracture, such as crack roughness, fractal dimension, and fragment size distribution. Based on our analysis, we suggest an explanation for the experimental observations of one- and two-mode power law distributions for fragments in the respective cases of fragmentation by high and low velocity impact.

ACKNOWLEDGMENTS

The authors gratefully acknowledge financial support from the ARO. The authors thank Dr. Alex Alexeev, Dr. Olga Kuksenok, and Dr. Victor Yashin for helpful discussions.

[1] L. Ponson, D. Bonamy, and E. Bouchaud, Phys. Rev. Lett. **96**, 035506 (2006).
[2] Phani Kumar V. V. Nukala, S. Zapperi, and S. Simunovic, Phys. Rev. E **74**, 026105 (2006).
[3] B. Skjetne, T. Helle, and A. Hansen, Phys. Rev. Lett. **87**, 125503 (2001).
[4] J. Schmittbuhl and K. J. Måløy, Phys. Rev. Lett. **78**, 3888 (1997).
[5] F. Kun, F. K. Wittel, H. J. Herrmann, B. H. Kröplin, and K. J. Måløy, Phys. Rev. Lett. **96**, 025504 (2006).
[6] T. Kadono and M. Arakawa, Phys. Rev. E **65**, 035107(R) (2002).
[7] J. A. Åström, B. L. Holian, and J. Timonen, Phys. Rev. Lett. **84**, 3061 (2000).
[8] B. B. Mandelbrot, D. E. Passoja, and A. J. Paullay, Nature (London) **308**, 721 (1984).
[9] *Statistical Models for the Fracture of Disordered Media*, edited by H. J. Herrmann and S. Roux (North-Holland, Amsterdam, 1990).
[10] E. D. Landau and E. M. Lifshitz, *Theory of Elasticity* (Pergamon Press, New York, 1986).
[11] L. Monette and M. P. Anderson, Modell. Simul. Mater. Sci. Eng. **2**, 53 (1994).
[12] T. Martin, P. Espanol, and M. A. Rubio, Phys. Rev. E **71**, 036202 (2005).
[13] A. Parisi and R. C. Ball, Phys. Rev. B **72**, 054101 (2005).
[14] O. Pla, F. Guinea, E. Louis, S. V. Ghaisas, and L. M. Sander, Phys. Rev. B **61**, 11472 (2000).
[15] T. Kadono, M. Arakawa, and N. K. Mitani, Phys. Rev. E **72**, 045106(R) (2005).
[16] Anders Meibom and Ivar Balslev, Phys. Rev. Lett. **76**, 2492 (1996).
[17] A. Diehl, H. A. Carmona, L. E. Araripe, J. S. Andrade, Jr., and G. A. Farias, Phys. Rev. E **62**, 4742 (2000).
[18] F. Wittel, F. Kun, H. J. Herrmann, and B. H. Kroplin, Phys. Rev. Lett. **93**, 035504 (2004).
[19] Hans J. Herrmann, Falk K. Wittel, and Ferenc Kun, Physica A **59**, 371 (2006).
[20] J. A. Astrom, F. Ouchterlony, R. P. Linna, and J. Timonen, Phys. Rev. Lett. **92**, 245506 (2004).
[21] J. A. Astrom, Adv. Phys. **55**, 247 (2006).